Mass, energy and economic analysis of supersonic CO2 separation for carbon capture, utilization and storage (CCUS)

Article

Published Version

Ding, H., Dong, Y., Zhang, Y., Wen, C. ORCID: https://orcid.org/0000-0002-4445-1589 and Yang, Y. (2024) Mass, energy and economic analysis of supersonic CO2 separation for carbon capture, utilization and storage (CCUS). Applied Energy, 373. 123856. ISSN 1872-9118 doi: https://doi.org/10.1016/j.apenergy.2024.123856 Available at https://centaur.reading.ac.uk/118675/

To link to this article DOI: http://dx.doi.org/10.1016/j.apenergy.2024.123856

Publisher: Elsevier

Applied Energy 373 (2024) 123856

Contents lists available at ScienceDirect

Applied Energy

journal homepage: www.elsevier.com/locate/apenergy

Mass, energy and economic analysis of supersonic CO_2 separation for carbon capture, utilization and storage (CCUS)

Hongbing Ding [a], Yuanyuan Dong [a], Yu Zhang [a], Chuang Wen [b,c,*], Yan Yang [b,*]

[a] Tianjin Key Laboratory of Process Measurement and Control, School of Electrical and Information Engineering, Tianjin University, Tianjin 300072, China
[b] Faculty of Environment, Science and Economy, University of Exeter, Exeter EX4 4QF, UK
[c] School of the Built Environment, University of Reading, Reading RG6 6AH, UK

HIGHLIGHTS

- Feasibility and prospect of supersonic CO_2 capture technology benefiting CCUS technology.
- A numerical model coupling Euler-Euler-Euler real gas model and entropy transport equation.
- The dual utilization of mass and energy by the CO_2 capture process in a CH_4-CO_2 binary system.
- System analysis and study of energy, entropy and exergy in the supersonic separator.
- Heterogeneous concentrations range in 5–7.5 kg/m^3 separate the most CO_2 and require the least energy.

ARTICLE INFO

Keywords:
CCUS
Carbon capture
CO_2 capture
Supersonic separation
Utilization of mass and energy
Climate change

ABSTRACT:

Accelerating global population growth and civilizational progress exacerbate energy demand, and global pressures involving decarbonization, energy poverty and fuel depletion force carbon-intensive countries to highlight carbon-negative carbon capture, utilization and storage (CCUS) technologies. As an emerging CCUS technology, its global applications hold great promise. However, the feasibility and prospects of supersonic CO_2 capture technology remain unclear, particularly regarding energy utilization. To this end, the entropy transport equation was innovatively introduced into the Euler-Euler-Euler real gas numerical model in the present study. The created model was utilized for simulating carbon capture in the CH_4-CO_2 system. To validate the accuracy of the developed model, a CO_2 condensation experiment and a supersonic separator experiment were used. Further, a series of simulations were conducted to investigate and quantify the mass and heat transfer for the CO_2 separation process in a supersonic separator. The results show that an inlet heterogeneous droplet mass concentration between 5 kg/m^3 and 7.5 kg/m^3 was expected to separate the most CO_2 mass and require the least energy. In addition, this study also investigated the economic parameters of different separation technologies and compared supersonic separation technology with other methods. In the future, major challenges in researching supersonic CO_2 capture technology will be to obtain ample experimental and simulation data, and to calculate the optimal structures and operating conditions.

1. Introduction

In the past few decades, accelerating global population growth and advancing civilization have led to the exponential growth in energy demand [1]. However, the primary contributor to the energy sector remains fossil energy [2], which worsens climate change and cannot ensure sustainable access to energy [3]. Global pressures related to the environment, energy poverty, decarbonization, and fuel depletion are forcing the exploration of renewable energy and the reduction of carbon utilization in high-carbon fuels [4]. Carbon capture, utilization, and storage (CCUS) technology is highly valued as a key carbon-negative technology by carbon-intensive countries [5], and it is highlighted as an essential solution with an emission reduction potential assessed by the International Energy Agency (IEA) as 6.9×10^9 t of CO_2 per year by 2070 under a sustainable development scenario, accounting for 19.27% of the total emission reduction [6].

CCUS technology, which separates and captures CO_2 from the

* Corresponding author at: Faculty of Environment, Science and Economy, University of Exeter, Exeter EX4 4QF, UK
E-mail addresses: c.wen@reading.ac.uk (C. Wen), yanyang2021@outlook.com, y.yang7@exeter.ac.uk (Y. Yang).

https://doi.org/10.1016/j.apenergy.2024.123856
Received 16 August 2023; Received in revised form 16 June 2024; Accepted 2 July 2024
Available online 16 July 2024

Nomenclature

a	heat transfer coefficient, W m^{-2} K^{-1}
b	sample value
c	Sound speed, m s^{-1}
C_{phase}	phase change constant, –
d	droplet diameter, m
D_w	cell-center-to-wall distance, m
E	total energy, J kg^{-1}
$\vec{F}_D$	drag force, kg m^{-2} s^{-2}
F_{sa}	safety factor, –
$\vec{g}$	gravity vector, m^{-1} s^{-2}
$\vec{g}_\tau$	gravity component parallel to film, m^{-1} s^{-2}
GCI	Grid Convergence Index
h	static enthalpy, J kg^{-1}
h_{lg}	latent heat, J kg^{-1}
I	homogeneous nucleation rate, m^{-3} s^{-1}
$\vec{J}$	diffusion flux, kg m^{-2} s^{-1}
k	turbulence kinetic energy, J kg^{-1}
K	bulk modulus of elasticity, Pa
m_m	molecular mass, kg
$\dot{m}$	mass change rate, kg m^{-3} s^{-1}
M	mass diffusivity of vapor, m^2 s^{-1}
n	droplet number concentration, m^{-3}
$\vec{n}$	film area normal, –
num	sample size, –
$\dot{N}_{col}$	source term due to collision, m^{-3} s^{-1}
p	fluid pressure, Pa
r	droplet radius, m
R_g	specific gas constant, J kg^{-1} K^{-1}
$RMSE$	root mean square error, –
s	specific entropy, J kg^{-1} K^{-1}
S	supersaturation, –
t	time, s
T	temperature, K
T_{sur}	film surface temperature, K
T_m	film half depth temperature, K
T_w	wall temperature, K
$\vec{u}$	velocity vector, m s^{-1}
u, v, w	velocity component, m s^{-1}
x, y, z	cartesian coordinates
Y	entropy generation rate, J m^{-3} s^{-1} K^{-1}
$\dot{Y}$	mass fraction, –

Greek

α	volume fraction, –
β^*	constant
γ	thermal diffusivity, m^2 s^{-1}
δ	film thickness, μm
ε	relative error of two meshes, –
ϵ	refinement factor ratio, –
ϑ	CO_2 molecule volume, m^3
κ_B	Boltzmann's constant, –
λ	thermal conductivity, W m^{-1} K^{-1}
μ	molecular dynamic viscosity, Pa s
ρ	density of mixture, kg m^{-3}
ρ_{hom}, ρ_{het}	homogeneous/heterogeneous droplet mass concentration, kg m^{-3}
σ	liquid surface tension, N m^{-1}
$\bar{\bar{\tau}}_{eff}$	effective stress tensor, Pa
$\vec{\tau}_{fs}$	viscous shear stress on gas-film interfaces, Pa
ω	specific dissipation rate, s^{-1}

Subscripts

A	due to aerodynamic losses
c	critical
col	collision and coalescence
C	due to heat conduction
CFD	computational fluid dynamics
d	deposition
D	due to viscosity
eff	effective
Exp	experiments
f	liquid film
g	gas
gen	entropy generation
het	heterogeneous
hom	homogenous
i	specie
in, out	inlet, outlet
l	liquid
L	due to phase change
m	mixture
ref	reference
sat	saturation
sur	surface
tu	turbulence
$tran$	entropy transfer
v	vapor

Superscripts

*	stagnation condition
–	Time-averaged
′	fluctuation
$\dot{p}$	order of algorithm accuracy

emission sources or the air, and delivers it to a suitable site for storage or recycling through cost-effective conversion [7], is acknowledged as an essential technology package for climate mitigation [8]. Recently, there has been a rapid maturation of CCUS-related technologies on a global scale, indicating a trend towards the emergence of new technologies and gradual drops in energy costs [9]. Fig. 1 summarizes various existing CCUS technology classes and outlines their pros and cons. Objectively speaking, absorption [10,11], adsorption [12,13], membrane [14,15], cyclone [16], cryogenics [17], and other technologies have been developed and proven effective for abatement in specific circumstances. However, research into supersonic separation technology began relatively recently, leaving uncertainties regarding its feasibility for decarbonization and ultimate application prospects. Therefore, this paper will focus on the challenges and potential opportunities for the development and promotion of this innovative technology.

Supersonic separation technology was initially patented in 1989 for air conditioning [18] and has evolved over the following decades to integrate the cooling properties of convergent-divergent nozzles with the centrifugal separation principle [19]. This integration utilizes swirling action to propel the condensed carbon droplets towards the wall and out [20]. In the late 1990s, two companies, Twister [21] and Translang [22], conducted structural, theoretical, simulation, and experimental research on this technology in parallel. Since then, other research institutions, including the Memorial University of Newfoundland [23], China University of Petroleum [24,25], and Beijing University of Technology [26] have also started to get involved in this field [27]. The supersonic separator depicted in Fig. 2(a) is a result of extensive research and testing [28]. It has undergone numerous iterations to

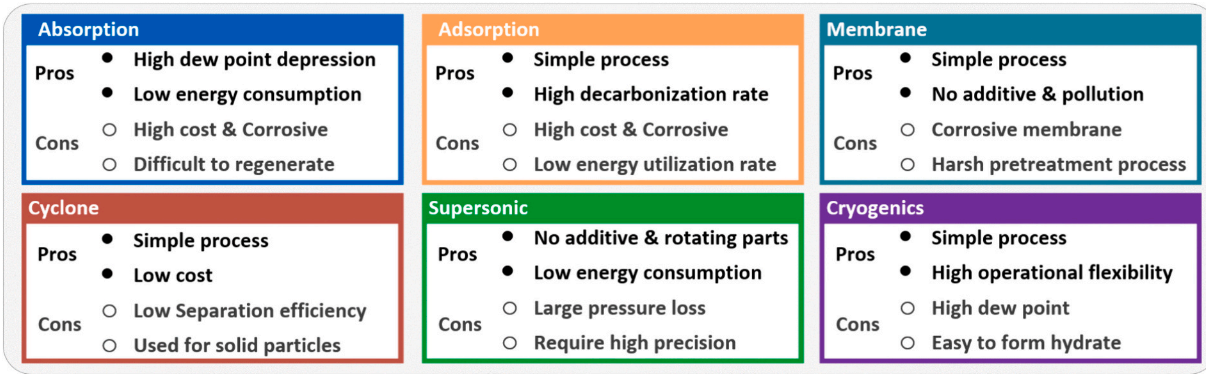

Fig. 1. Pros and cons of existing CCUS technology.

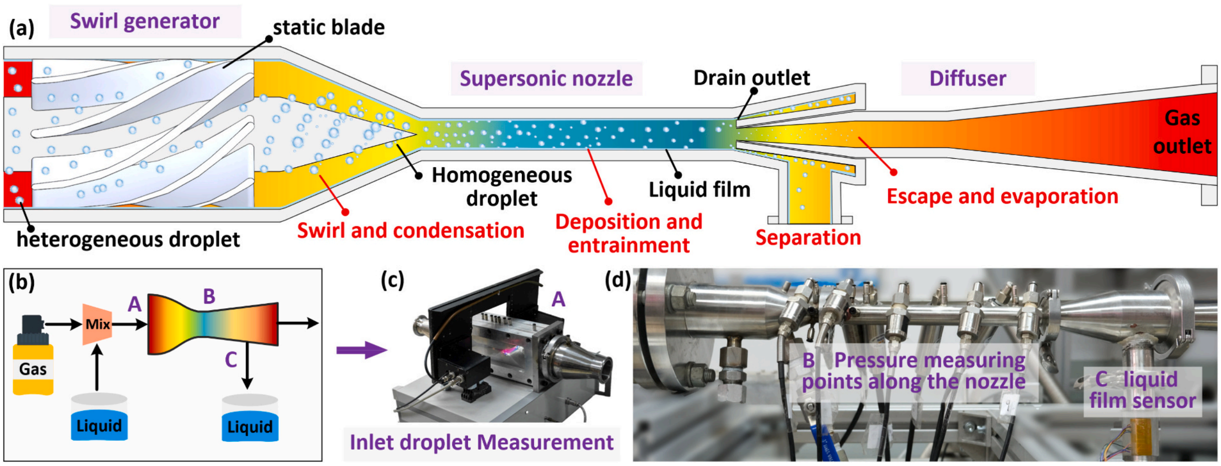

Fig. 2. Supersonic separator: (a) working mechanism; (b) experimental platform; (c)(d) measuring means.

achieve its current design [29]. The swirl-condensation-separation dehumidification step is considered to have a good dew point depression, which is beneficial to gas-liquid separation. Further, to understand the working principle and performance of supersonic separators, it is critical to grasp the condensation and swirling processes involved, which can be achieved through numerical studies. Liu et al. [30] developed an Euler-Euler mathematical model of a methane-vapor binary system, as a way to study the energy separation and condensation characteristics of wet natural gas. Their finding is that pressure energy recovery efficiency in the range of 57.1%–64.2% ensures high liquefaction efficiency of natural gas in actual natural gas processing. Shooshtari et al. [31] developed an Euler-Euler model considering homogeneous/heterogeneous condensation to study the effect of heterogeneous salt particles on the process of condensation and separation in a supersonic separator. Bai et al. [32] utilized Euler-Lagrange method to simulate crucial features of supersonic branching flow. In a similar vein, Wang et al. [33] harnessed the Euler-Lagrange model to forecast droplet trajectory and separation efficiency within supersonic separators. The study shows that steam separation is significantly affected by droplet diameters that fall within the 2–4 μm range. Combining both the Euler-Euler and the Euler-Lagrange approaches provides a comprehensive understanding of gas and droplet behaviors. The Euler-Euler approach considers macroscopic droplet information, while the Euler-Lagrange approach locates discrete droplet information.

In recent years, there has been progress in introducing the Euler film model into the intrinsic framework, allowing for accurate simulation of the liquid film spreading on the wall [34,35]. Yue et al. [36] investigated the sensitivity of liquid flow rate to liquid film flow in a Gas-Liquid Cylindrical Cyclone using the Euler-Euler-Euler model. Their findings suggest that increased liquid flow rates impact the uniformity of the liquid film distribution. Meanwhile, Deng et al. [37] simulated the gas-liquid separation process within an axial flow cyclone by utilizing both the Euler-Lagrange method and the Euler film model. The outcomes reveal a progressive coverage of the separation section by the liquid film over time. Ding et al. [29,38] introduced these two methods into the supersonic separator, respectively, and analyzed the condensation and separation performance from both continuous and discrete perspectives, and obtained some key factors affecting the separation efficiency. Meanwhile, a joint model integrating the Euler-Euler-Euler model and the NIST real gas EOS has been developed to analyze the effect of supercritical CO_2 capture under different conditions [39]. The discussion focuses on the condensation characteristics of the pure CO_2 system, as well as the mass separation characteristics of the CH_4-CO_2 system. Additionally, the impact of heterogeneous droplet concentration on mass separation is also explored. In addition to mass separation, energy loss is also crucial for assessing the performance of supersonic separators, of which entropy analysis is a commonly utilized method for this purpose [40]. However, previous research has not extensively addressed the energy and entropy aspects, and thus is necessarily insufficient to comprehensively assess the decarbonization capability of supersonic separators.

The purpose of this study is to assess the potential of supersonic CO_2 capture technology for high pressure decarbonization using an integrated model that incorporates the entropy transport equation into the Euler-Euler-Euler real gas model, focusing on the mass, energy and economic analysis of the separation process while discussing entropy generation and exergy destruction. Heterogeneous droplet concentration is still considered a factor for sensitivity analysis with the aim of improving condensation and separation. The direction of optimization and potential applications for supersonic CO_2 capture technology are also presented in terms of numerical simulation.

2. Supersonic CO_2 capture technology

2.1. Working mechanism

The supersonic separator employs two processes to perform gas-liquid separation, namely low-temperature condensation and cyclone separation [41]. The low-temperature condensation process creates a low-temperature environment by expanding the nozzle, resulting in the condensation of vapor into droplets. Cyclone separation refers to the process that the static blades on the guide cone with a certain diversion angle have an influence on the internal flow field, resulting in a centrifugal speed, so that the droplets with large mass are centrifuged to the wall and gas-liquid separation is realized [42]. Fig. 2(a) is a conceptual diagram of a typical supersonic separator, and Fig. 2(d) is the corresponding object. A supersonic separator mainly consists of a swirl generator, a supersonic nozzle, and a diffuser. A mixture of methane (CH_4) and CO_2 enters the swirl generator and becomes swirled. The swirling gas is accelerated and cooled in the convergent section of the supersonic nozzle to create a condensing environment. In the divergent section of the supersonic nozzle, the CO_2 vapor condenses into droplets that are thrown against the wall and spread out to form a liquid film under the action of the swirl.

Ideally, the produced liquid film flows along the wall outside the liquid outlet, and only dry gas containing methane enters the diffuser, where pressure is restored. However, it is important to note that steam is not completely condensed into droplets, and not all droplets are large enough to be separated by centrifugation. Small droplets will evaporate and escape into the diffuser. Additionally, the liquid film formed by droplet deposition can be stripped and entrained to the gas core. All of these factors will impact the actual separation efficiency. Heterogeneous droplets refer to externally introduced droplets that provide condensation cores to the supersonic separator. Contrastingly to homogeneous droplets, when a non-equilibrium condensation environment takes place, foreign cores can grow directly, without the need for steam to form the core through condensation. The external core's diameter surpasses that of the homogeneous condensation core, providing centrifugal separation with greater benefits. Previous studies have shown that introducing heterogeneous droplets is an effective method to increase the separation efficiency of a supersonic separator for mass separation purpose [39]. However, the qualitative and quantitative analysis of the entropy generation distribution and the energy distribution in the supersonic separator has not been carried out yet. Therefore, the entropy transport equation is added to the existing model, and the entropy generation in the supersonic separator is intensively studied.

2.2. Numerical model

All mathematical equations and the CFD implementation will be presented in this section and the following section 2.3. As mentioned above, the model developed in this paper introduces the entropy transport equation to the Euler-Euler-Euler model, which distinguishes this study from other literature related to supersonic separators. As shown in Fig. 3 the flow field within the supersonic separator was evaluated via the Euler-Euler-Euler approach. The governing equations for the gas and liquid phases were Eulerian, while the exchange of source terms, such as evaporation and condensation, was taken into account. The Euler film model was utilized to compute the formation and development of the liquid film and the phase change of gas and droplets on the liquid film, to determine the information at the wall. Additionally, to evaluate the thermodynamic and transport properties of a mixture of CH_4 and CO_2, the NIST real gas model was employed [43]. In detail, the thermodynamic properties were calculated using the mixing rules of the Helmholtz-energy EOS applied to the mixture components [44]. Furthermore, the introduction of the entropy transport equation enabled the calculation of entropy generation resulting from aerodynamic losses, viscosity, heat conduction, and phase change.

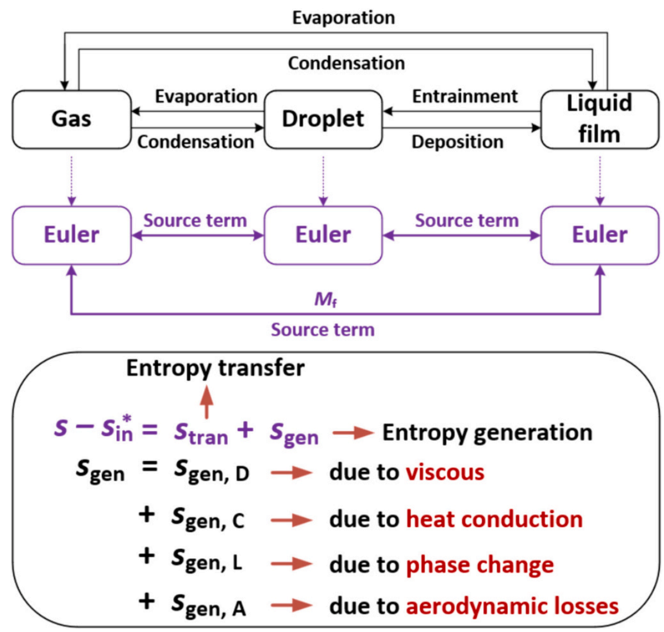

Fig. 3. Schematic: mathematical model and entropy generation.

2.2.1. The Euler-Euler-Euler model

The developed Euler-Euler-Euler model is a three-field, two-phase model consisting of a gas phase and liquid phase, with the fields comprising the gas, droplet, and liquid film [29]. Each field is governed by its own equations, and interactions between the fields are accounted for, including non-equilibrium phase transitions between gas and droplet, deposition between droplet and liquid film, and condensation and evaporation between gas and liquid film. Mass changes are converted among the three fields through source terms.

All the details of the governing equations can be found in Table 1. The conservation equations for mass, momentum, and energy in a gas-phase mixture of CH_4 and CO_2, along with the species transport equation between CH_4 and CO_2 gases, are presented in **Eq. (1) - Eq. (4)**. For the CO_2 droplets, the governing equations include the droplet mass conservation equation, the droplet momentum conservation equation, and the droplet number concentration transport equation, corresponding to **Eq. (5) - Eq. (7)** in Table 1. For a supersonic separator, the presence of the swirling field causes the droplets to impinge on the tube wall and transform into a liquid film, and the liquid film conservation equations are given by **Eq. (8) - Eq. (10)**.

In Table 1, $\dot{m}_{hom}$, $\dot{m}_{het}$, $\dot{m}_d$, and $\dot{m}_f$ represent the source terms resulting from phase interactions that ensure mass conservation across two phases and three fields, **Eq. (11) - Eq. (14)** in Table 2 are the calculation formulas for them. $\dot{m}_{hom}$, $\dot{m}_{het}$ represent the mass source term produced by gas non-equilibrium condensation or homogeneous/heterogeneous droplet evaporation, $\dot{m}_d$ represents the mass source term produced by droplet deposition to form a liquid film, and $\dot{m}_f$ represents the mass source term produced by film evaporation or gas condensation to liquid film. In particular, for the calculation of important parameters for droplet nucleation and growth during non-equilibrium phase transition process, a detailed description is also given in Table 2. **Eq. (15)** is the formula for calculating the nucleation rate (m^{-3} s^{-1}) of a homogeneous droplet, where the critical nucleation radius is obtained from **Eq. (16)**. **Eq. (18)** is a formula for calculating the growth rate of a homogeneous or heterogeneous droplet, wherein the radius of the homogeneous or

Table 1
Summary of the governing equations for gas, droplets and liquid film

Item	Equation	
Gas phase	$\frac{\partial}{\partial t}(\alpha_g\rho_g) + \nabla\bullet\left(\alpha_g\rho_g\vec{u}_g\right) = -\left(\dot{m}_{hom}+\dot{m}_{het}\right)$	(1)
	$\frac{\partial}{\partial t}\left(\alpha_g\rho_g\vec{u}_g\right) + \nabla\bullet\left(\alpha_g\rho_g\vec{u}_g\vec{u}_g\right) = -\alpha_g\nabla p + \nabla\bullet\left(\alpha_g\bar{\bar{\tau}}_{eff}\right) + \alpha_g\rho_g\vec{g} - \left(\dot{m}_{hom}+\dot{m}_{het}\right)\vec{u}_g - \vec{F}_D$	(2)
	$\frac{\partial}{\partial t}(\alpha_g\rho_g E) + \nabla\bullet\left[\alpha_g(\rho_g E+p)\vec{u}_g\right] = \nabla\bullet\left[\alpha_g\lambda_{eff}\nabla T_g - \alpha_g\sum_i h_i\vec{J}_i + \alpha_g\left(\bar{\bar{\tau}}_{eff}\bullet\vec{u}_g\right)\right] - \left(\dot{m}_{hom}+\dot{m}_{het}\right)h_{lg}$	(3)
	$\frac{\partial}{\partial t}\left(\alpha_g\rho_g\dot{Y}_i\right) + \nabla\bullet\left(\alpha_g\rho_g\vec{u}_g\dot{Y}_i\right) = -\nabla\bullet\left(\alpha_g\vec{J}_i\right) - \left(\dot{m}_{hom}+\dot{m}_{het}\right)$	(4)
Droplets	$\begin{cases}\frac{\partial}{\partial t}(\alpha_{hom}\rho_l) + \nabla\bullet\left(\alpha_{hom}\rho_l\vec{u}_{hom}\right) = \dot{m}_{hom} - \dot{m}_{col} \\ \frac{\partial}{\partial t}(\alpha_{het}\rho_l) + \nabla\bullet\left(\alpha_{het}\rho_l\vec{u}_{het}\right) = \dot{m}_{het} + \dot{m}_{col}\end{cases}$	(5)
	$\begin{cases}\frac{\partial}{\partial t}\left(\alpha_{hom}\rho_l\vec{u}_{hom}\right) + \nabla\bullet\left(\alpha_{hom}\rho_l\vec{u}_{hom}\vec{u}_{hom}\right) = -\alpha_{hom}\nabla p + \alpha_{hom}\rho_l\vec{g} + \left(\dot{m}_{hom}-\dot{m}_{col}\right)\vec{u}_{hom} + \vec{F}_{D,hom} \\ \frac{\partial}{\partial t}\left(\alpha_{het}\rho_l\vec{u}_{het}\right) + \nabla\bullet\left(\alpha_{het}\rho_l\vec{u}_{het}\vec{u}_{het}\right) = -\alpha_{het}\nabla p + \alpha_{het}\rho_l\vec{g} + \left(\dot{m}_{het}+\dot{m}_{col}\right)\vec{u}_{het} + \vec{F}_{D,het}\end{cases}$	(6)
	$\begin{cases}\frac{\partial n_{hom}}{\partial t} + \nabla\bullet\left(n_{\mathrm{hom}}\vec{u}_{hom}\right) = I - \dot{N}_{col} \\ \frac{\partial n_{het}}{\partial t} + \nabla\bullet\left(n_{het}\vec{u}_{het}\right) = 0\end{cases}$	(7)
Liquid film	$\frac{\partial}{\partial t}(\rho_l\delta) + \nabla_{sur}\bullet\left(\rho_l\delta\vec{u}_f\right) = \delta\left(\dot{m}_d - \dot{m}_f\right)$	(8)
	$\frac{\partial}{\partial t}\left(\rho_l\delta\vec{u}_f\right) + \nabla_{sur}\bullet\left(\rho_l\delta\vec{u}_f\vec{u}_f\right) = = -\delta\nabla_{sur}p + \rho_l\delta\vec{g}_\tau + \frac{3}{2}\vec{\tau}_{fs} - \frac{3\mu_l\vec{u}_f}{\delta} + \vec{F_d} + \left(\dot{m}_d - \dot{m}_f\right)\vec{u}_f$	(9)
	$\frac{\partial}{\partial t}(\rho_l\delta h_f) + \nabla_{sur}\bullet\left(\rho_l\delta h_f\vec{u}_f\right) = \frac{\lambda_l}{\delta}(T_{sur} + T_w - 2T_m) + \left(\dot{m}_d - \dot{m}_f\right)h_{lg}$	(10)

Table 2
Summary of the source terms for gas, droplets and liquid film

Equation	
Source term between gas and droplet [45]: $\dot{m}_{hom} = I\rho_l\frac{4\pi r_c^3}{3} + n_{\mathrm{hom}}\rho_l 4\pi r_{hom}^3\frac{dr_{hom}}{dt}$	(11)
Source term between gas and droplet: $\dot{m}_{het} = n_{het}\rho_l 4\pi r_{het}^3\frac{dr_{het}}{dt}$	(12)
Source term between droplet and film [46]: $\dot{m}_d = \dot{m}_{d,hom} + \dot{m}_{d,het} = \alpha_{hom}\rho_l\vec{u}_{hom}\bullet\vec{n} + \alpha_{het}\rho_l\vec{u}_{het}\bullet\vec{n}$	(13)
Source term between gas and film [47]: $\dot{m}_f = \frac{1}{\delta}\frac{\rho_g M/D_w}{\rho_g M/D_w + C_{phase}}C_{phase}\left(\dot{Y}_{sat} - \dot{Y}\right)$	(14)
Homogeneous nucleation rate [48]: $I = \frac{\vartheta\rho_g^2}{S}\sqrt{\frac{2\sigma}{\pi m_m^5}}exp\left(-\frac{16\pi}{3}\frac{\vartheta^2\sigma^3}{(\kappa_B T_g)^3(ln(S))^2}\right)$	(15)
Critical nucleation radius: $r_c = \frac{2\sigma}{\rho_l R_g T_g ln(S)}$	(16)
Droplet radius: $r_{hom} = \left(\frac{3\alpha_{\mathrm{hom}}}{4\pi n_{\mathrm{hom}}}\right)^{\frac{1}{3}}, r_{het} = \left(\frac{3\alpha_{het}}{4\pi n_{het}}\right)^{\frac{1}{3}}$	(17)
Droplet growth rate [49]: $\frac{dr}{dt} = \frac{\sum_{i=1}^2 a_i}{\rho_l h_{lg}}\left(T_{sat} - T_v - (T_{sat} - T_g)\frac{r_c}{r}\right)$	(18)

heterogeneous droplet is obtained from **Eq. (17)**.

2.2.2. *Entropy transport equation*

Furthermore, the entropy transport equation was introduced to advance this study. The specific entropy s of wet vapor in a transonic condensing flow can be expressed as [50]

$$s - s_{in}^* = s_{tran} + s_{gen} = s_{tran} + s_{gen,D} + s_{gen,C} + s_{gen,L} + s_{gen,A} \quad (19)$$

where s_{tran} stands for entropy transfer. The total entropy generation s_{gen} consists of four components ($s_{gen,D}$, $s_{gen,C}$, $s_{gen,L}$, $s_{gen,A}$), representing the entropy generation due to viscosity, heat conduction, phase change, and aerodynamic losses, Table 3 is the specific equations. The transport equations for entropy are first-order linear partial differential equations (PDEs) that satisfy the principle of superposition, each part of entropy change is calculated by **Eq.(20)**. The equations for the source terms Y_{tran}, $Y_{gen,D}$, $Y_{gen,C}$, and $Y_{gen,L}$ that correspond to s_{tran}, $s_{gen,D}$, $s_{gen,C}$, and $s_{gen,L}$ can be found in **Eq. (21)-Eq. (28)**. The viscous dissipation $Y_{gen,D}$ appears two groups of terms, one with mean and the other with fluctuating quantities, namely local viscous entropy generation rate. The entropy generated during a condensed phase transition is denoted by $s_{gen,L}$, which is caused by the temperature difference between the liquid and vapor. Therefore, $Y_{gen,L}$ is also linked to the temperatures of both gas and liquid. After completing calculations for the other variables, subtracting their sum from the total provides the result for $s_{gen,A}$.

It is worth pointing out that in this mathematical model, the

Table 3
Summary of the formulas for calculating the entropy change

Item	Equation	
General	$\rho\frac{D(s_\phi)}{Dt} = \frac{\partial \rho s_\phi}{\partial t} + \frac{\partial}{\partial x_i}\left(\rho s_\phi \vec{u}_i\right) = Y_\phi$	(20)
s_{tran}	$Y_{tran} = \frac{\partial}{\partial x_i}\left(\frac{\lambda_{eff}}{T}\frac{\partial T}{\partial x_i}\right)$	(21)
$s_{gen,D}$	$Y_{gen,D} = Y_{gen,\overline{D}} + Y_{gen,D'}$	(22)
	$Y_{gen,\overline{D}} = \frac{\mu}{T}\left[2\left\{\left(\frac{\partial \overline{u}}{\partial x}\right)^2 + \left(\frac{\partial \overline{v}}{\partial y}\right)^2 + \left(\frac{\partial \overline{w}}{\partial z}\right)^2\right\} + \left(\frac{\partial \overline{u}}{\partial y} + \frac{\partial \overline{v}}{\partial x}\right)^2 + \left(\frac{\partial \overline{u}}{\partial z} + \frac{\partial \overline{w}}{\partial x}\right)^2 + \left(\frac{\partial \overline{v}}{\partial z} + \frac{\partial \overline{w}}{\partial y}\right)^2\right]$	(23)
	$Y_{gen,D'} = \frac{\rho\beta^* k\omega}{\overline{T}}$	(24)
$s_{gen,C}$	$Y_{gen,C} = Y_{gen,\overline{C}} + Y_{gen,C'}$	(25)
	$Y_{gen,\overline{C}} = \frac{\lambda}{\overline{T}^2}\left[\left(\frac{\partial \overline{T}}{\partial x}\right)^2 + \left(\frac{\partial \overline{T}}{\partial y}\right)^2 + \left(\frac{\partial \overline{T}}{\partial z}\right)^2\right]$	(26)
	$Y_{gen,C'} = \frac{\gamma_{tu}}{\gamma}\frac{\lambda}{\overline{T}^2}\left[\left(\frac{\partial \overline{T}}{\partial x}\right)^2 + \left(\frac{\partial \overline{T}}{\partial y}\right)^2 + \left(\frac{\partial \overline{T}}{\partial z}\right)^2\right]$	(27)
$s_{gen,L}$	$Y_{gen,L} = \left(\dot{m}_{hom} + \dot{m}_{het}\right) \bullet h_{lg}\left(\frac{1}{T_g} - \frac{1}{T_l}\right)$	(28)

thermodynamic properties are calculated using the modified Benedict-Webb-Rubin (MBWR) EOS, Helmholtz-energy EOS, and extended corresponding states (ECS) triplet equations of state provided by the NIST model for the pure CO_2 system, and the mixing rules of the CH_4-CO_2 system, the thermodynamic properties were calculated using the mixing rule of Helmholtz-energy EOS.

2.3. Numerical schemes

Numerical calculations were performed in this study utilizing Ansys Fluent software. A combination of default solver and user-defined functions was utilized. User-defined functions (UDFs) are written to compute the droplet governing equations, the coupled source terms of the two-phase three-field models, and the entropy transport equation using the UDS equations, and the UDM is used to store the values of the relevant physical quantities. The turbulence model uses the standard k-epsilon model when the simulation object is a Laval nozzle and the Reynolds stress model (RSM) when the simulation object is a supersonic separator, bringing a heightened level of accuracy to the simulation. A pressure-based transient solver utilizing implicit formulation and the Roe-FDS flux type solution is employed. The governing equations, the turbulent kinetic energy equation, and the turbulent dissipation rate equation were calculated using the second-order upwind equation. To solve the droplet deposition problem, the coupling between the wall and the Eulerian wall film model is turned on in order to compute the liquid film formation and evolution problem. The boundary conditions are similar to the operation conditions, where the pressure inlet condition is applied to the inlet of working fluid, while the pressure outlet condition is applied to the outlet of working fluid. The detailed boundary conditions are listed in Table 4. Furthermore, the numerical model is based on the following considerations and assumptions [39]:

(1) The condensation characteristics of CO_2 in pure CO_2 flow are studied by using pure CO_2 system, and the CO_2 capture process in natural gas is simulated by using CH_4- CO_2 system.
(2) Assuming that all droplets are spherical, consider coalescence and collision between droplets.
(3) Considering the homogeneous and heterogeneous condensations of CO_2 vapor, it is assumed that the latent heat released by condensation is absorbed by the gas phase.
(4) Considering the slip between gas phase and liquid phase, the phase change between gas phase and liquid film, and the deposition and entrainment between liquid droplets and liquid film.

3. Validation and analysis

The model was subjected to two validation processes, the first focused on demonstrating the model's ability to accurately predict CO_2 condensation, and the second aimed to assess the accuracy of the model's prediction of the combined performance of the supersonic separator. In addition, classical variables such as pressure and temperature are analyzed to illustrate the rationale for numerical and geometric modeling.

3.1. Validation of the condensation model

Fig. 4 (a) shows the structure and mesh of the supersonic nozzle used for the validation from the CO_2 condensation experiment of Lettieri et al. [51]. The experimental data of pressure ratio also comes from this

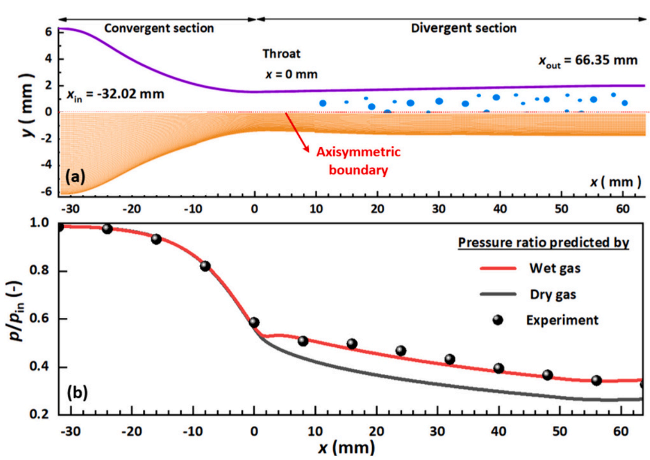

Fig. 4. Validation: (a) structure and mesh; (b) comparison (The data comes from [51]).

Table 4
Boundary conditions

Term	Boundary conditions	Mathematical description	Constraint for
Gas	Inlet	$p_{in} = p_{total}, T_{in} = T_{total}$	Eqs. (1)–(3)
	Outlet	$p_{out} = p_{static}, T_{out} = T_{static}$	
	Wall	$\vec{u}_g = 0, \frac{\partial T}{\partial n_w} = 0$	Eqs. (2)–(3)
Component	Inlet	$\dot{Y}_i = \text{const.}$	Eq. (4)
Droplet	Inlet	$\alpha_{hom} = 0, \vec{u}_{hom} = 0, n_{hom} = 0$ $\alpha_{het} = \text{const.}, \vec{u}_{het} = \vec{u}_g, n_{het} = \text{const.}$	Eqs. (5)–(7)
	Outlet	$\frac{\partial \alpha}{\partial z} = 0, \frac{\partial u}{\partial z} = 0, \frac{\partial n}{\partial z} = 0$	
	Coupled with wall film	wall flux : $\left(\alpha_{hom}\rho_l \vec{u}_{hom} + \alpha_{het}\rho_l \vec{u}_{het}\right) \bullet \vec{n}$	Eqs. (5)–(10)

document. The total length of the nozzle was 98.37 mm with inlet, throat and outlet diameters of 12.70 mm, 3.09 mm and 4.01 mm, respectively. A two-dimensional structural mesh was used with localized refinement of the region near the wall and throat. Half of the mesh was drawn, and the axes were used as axisymmetric boundaries to patch the entire flow field.

A verification test was performed first to obtain the optimal computational mesh, three sets of meshes were computed and analyzed using the Grid Convergence Index (GCI): I: fine mesh (87,200 quadrilateral cells), II: medium mesh (71,880 quadrilateral cells), and III: coarse mesh (56,200 quadrilateral cells).The GCI was computed using **Eq.(29)**, where F_{sa} is the safety factor with an empirical parameter value of 3, ε is the relative error between two meshes, ϵ is the refinement factor ratio, and the superscript $\dot{p}$ is the order of algorithm accuracy. Accurate prediction of condensation shockwave and the outlet wetness in a supersonic nozzle are the measures of grid quality. The two-parameter grid independence test is carried out by using the condensation shock wave position (Wilson point) and outlet wetness in supersonic nozzle, specific GCI test results are shown in Table 5.

$$GCI = \frac{F_{sa}|\varepsilon|}{\epsilon^{\dot{p}} - 1} \times 100\% \quad (29)$$

The present computational fluid dynamics (CFD) simulation maintains the same pressure and temperature conditions as Lettieri's [51] experiments, with the inlet pressure and temperature set to p_{in}= 57.24 atm and T_{in} = 314.78 K. Fig. 4 (b) shows a comparison of the CFD results with the experimental results. The CFD model accurately predicted both the Wilson point and the condensation shock wave for the wet gas condensation process. The CFD model's prediction accuracy is reflected in the root mean square error (RMSE), as calculated by **Eq. (30)**, producing a result of 0.01471 (close to 0). Thus, the CFD results and experimental results are in good agreement.

$$RMSE = \sqrt{{}^{1}\!/_{num}\sum_{i=1}^{num}\left(b_{i,CFD} - b_{i,Exp}\right)^2} \quad (30)$$

3.2. Validation of supersonic separator

Next, the CFD model was validated to assess the adequacy of the developed model to evaluate the overall performance of the supersonic separator. Currently, there is a gap in the experiments on CO_2 condensation and separation in supersonic separators. And the existing experimental conditions support to be performed in an air-water system. The experimental concept is shown in Fig. 2(b), the mixture of wet gas and heterogeneous water droplets enters the supersonic separator. A water collection device is placed at the liquid outlet and the dry gas is discharged from the dry gas outlet. Three measurement methods were employed during the experiment, and physical photographs are included in are shown in Fig. 2(c-d). Measurement method A aims to measure the size and concentration of water droplets, and uses the principle of extinction, Method B is designed to measure the wall pressure along the supersonic nozzle using pressure probes, while Method C measures the liquid film thickness at the liquid outlet.

The structure of the used supersonic separator is shown in Fig. 5. The swirl generator consists of the guide cone and 8 static blades, and each blade has a length of 80 mm, a height of 13.5 mm, and a thickness of 3 mm. There is a 65 mm distribution region in front of the blade region and a 10 mm straight section behind the blade region which connects to the supersonic nozzle. The supersonic nozzle features a 50 mm convergent section and a 265 mm divergent section. Additionally, a 15 mm straight section is included post-throat to satisfy installation requirements. The nozzle inlet, throat, and outlet have diameters of 54 mm, 11.57 mm and 14.60 mm respectively. The supersonic nozzle is succeeded by a drain section and a diffuser. The drain section measures 50 mm in length and has a clearance of 2 mm at the drain outlet. The total length of the diffuser is 480 mm, which diameter is expanded from 12.60 mm to 16.90 mm and finally reaches 54 mm. The same geometric configuration is applied in both the experimental and simulation procedures in order to guarantee precision of validation, the overall structure can also be seen from the mesh diagram in Fig. 5. In order to optimize computing resources, the first 50 mm of distribution region, which has little effect on accuracy, has been omitted. The z-axis was set as the axis of rotation and the throat center was set as the position of origin. By conducting GCI tests, the number of grid cells was determined to be 557,560.

On this basis, experiments and simulations were performed with air and water vapor in the gas phase and water droplets in the liquid phase. The operating conditions adopted were that, the inlet and outlet pressures were 3 atm and 1 atm, the inlet and outlet temperatures were 300 K, the inlet humidity was 100%, and the inlet heterogeneous droplet diameter and mass concentration were 2.2 μm and 0.005 kg/m^3. Fig. 6 (a) shows the gas pressure distribution obtained from the experiment and the CFD model. The experimental data in the figure are in good agreement with the CFD data, and the *RMSE* is evaluated as 0.04772, indicating a high agreement. The comparison was continued by changing the inlet heterogeneous droplet mass concentration $\rho_{het,in}$ to 0.05 kg/m^3 and 0.1 kg/m^3. Fig. 6(b) shows the CFD and experimental data for the film thickness at the liquid outlet. Such deviations of CFD results from experimental results are considered to be within a reasonable range due to the inherent uncertainty and volatility of the liquid film data. In summary, the CFD model can be used for further analysis.

Table 5
The specific test results of the Grid Convergence Index.

			Grid I-II		Grid II-III	
	F_{sa}	$\dot{p}$	$\varepsilon_{I,II}$ (%)	$GCI_{I,II}$ (%)	$\varepsilon_{II,III}$ (%)	$GCI_{II,III}$ (%)
Position	3	3	0.15	0.19	0.81	1.02
Outlet wetness	3	3	0.13	0.34	0.69	1.48

3.3. Analysis of classical variables

The classical variables for CH_4-CO_2 system in this supersonic separator were analyzed and captured using the developed model. The data presented in Fig. 7 arises from the case for inlet, gas outlet, and liquid outlet pressure of 150 atm, 80 atm, and 60 atm, respectively, in combination with a temperature of 258 K. The inlet heterogeneous droplet diameter and the inlet heterogeneous mass concentration were determined to be 10 μm and 7.5 kg/m^3. The molar concentration of CO_2 at the inlet is 1.1 kmol/m^3, 1.7 kmol/m^3 and 2.3 kmol/m^3 respectively. Except for studying the influence of molar concentration of CO_2 at the inlet on condensation, the other numerical simulations all adopt 2.3 kmol/m^3 as the condition of fixed molar concentration of CO_2. And, Fig. 9 and Fig. 10 depict mass-averaged statistical distributions of pressure, temperature, droplet number concentration, sound speed, and Mach number along the supersonic separator, revealing an overall trend. Before starting, two aspects of the model need to be emphasized: firstly, the technique used to calculate the Mach number, and secondly, the inclusion of dry-ice formation.

Then, three cases where the molar concentration of CO_2 at the inlet is 1.1 kmol/m^3, 1.7 kmol/m^3 and 2.3 kmol/m^3 respectively were selected, and the typical flow field parameters under the three concentrations were analyzed: the contour distribution of CO_2 mole fraction (Fig. 8(a)) and the evolution trend of supercooling (Fig. 8(b)). The results show that with the increase of imported carbon dioxide molar concentration, the trend of the CO_2 mole fraction is basically the same, showing a trend of first decreasing and then slightly increasing. In addition, with the increase of imported molar concentration, the supercooling required for condensation decreases, and condensation will be more likely to occur. This is because the greater the molar fraction of imported CO_2 vapor, the greater the partial pressure of CO_2 in the gas mixture, the easier it is for CO_2 to condense, and the more CO_2 it condenses.

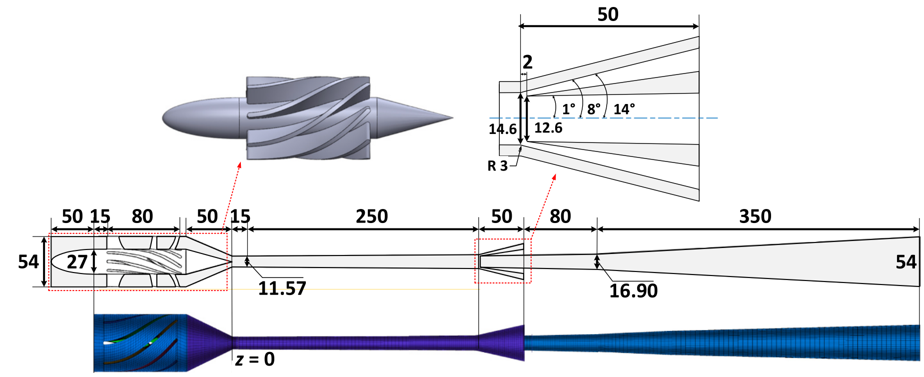

Fig. 5. Structure and mesh of the supersonic separator.

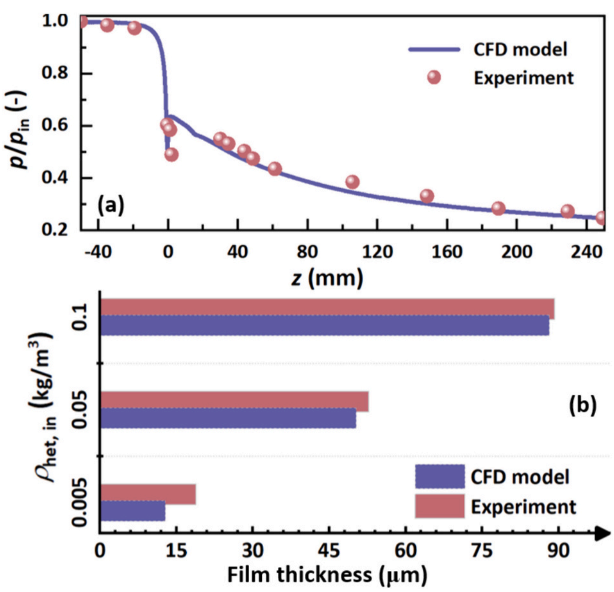

Fig. 6. Validation: (a) comparison of pressure along the nozzle; (b) comparison of film thickness.

The determination of subsonic/supersonic conditions for compressible multiphase flows relies on the Mach number calculation. It should be noted that the Mach number of a fluid mixture composed of two phases cannot be reduced to a single-phase ideal gas model [52]. In this work, the calculation of the compressible gas phase sound speed c_g, whether single or multi-species, follows the real gas model. For the compressible liquid phase, the sound speed of the liquid is given by [53]

$$c_l = \left(\frac{\rho_{l,ref}}{K_l} exp\left(\frac{p_l - p_{l,ref}}{K_l}\right)\right)^{-\frac{1}{2}} \tag{31}$$

where K_l is the liquid bulk modulus of elasticity, $\rho_{l,ref}$ and $p_{l,ref}$ are the reference density and pressure of the liquid. The relation between the mixture sound speed and the single-phase sound speed is:

$$c_m^2 = \left(\frac{\alpha_g}{\rho_g} + \frac{\alpha_l}{\rho_l}\right)\left(\frac{\alpha_g}{\rho_g c_g^2} + \frac{\alpha_l}{\rho_l c_l^2}\right)^{-1} \tag{32}$$

If $\alpha_l = 0$, meaning there is no liquid present in the flow field, the result of c_m is c_g. If α_l is greater than zero, c_m usually exceeds the speed of c_g. Therefore, determining the mixture sound speed is crucial, and cannot be substituted with the sound speed in a single phase. The Mach number is thus calculated by dividing the mixture speed by the mixture sound speed, denoted as $Ma = \left|\vec{u}_m\right|/c_m$ [54]. During the design of the supersonic separator, the goal was to avoid shockwaves within the supersonic nozzle. The length of the nozzle's divergent section was determined to be 250 mm. As a result, Fig. 7(a) and Fig. 9 clearly show that the occurrence of pressure shockwaves is precisely at the drain outlet. The maximum Mach number upstream of the shock at axial position $z = 265$ mm is 1.53, where the minimum pressure is 28.75 atm.

CO_2 freeze-out occurs when CO_2 is cooled below the CO_2 triple-phase point temperature (217 K). This phenomenon poses a problem in CO_2 capture as dry ice can cause blockages in supersonic separators. As a

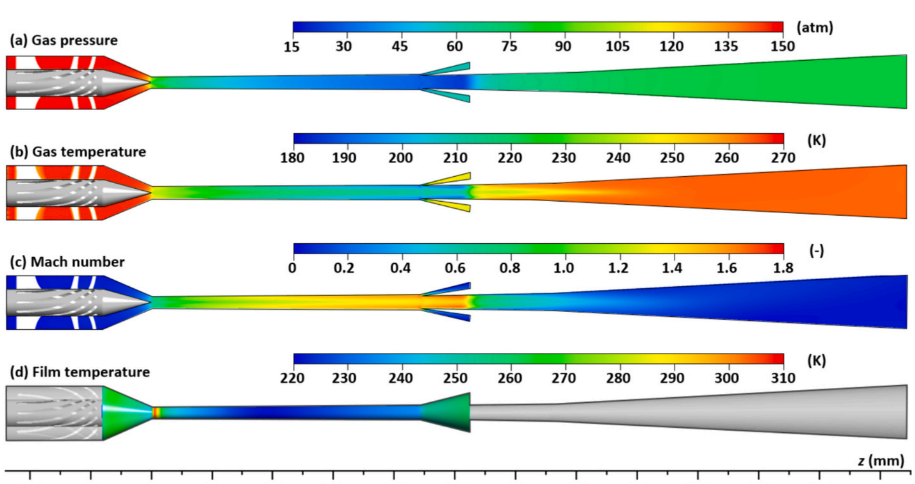

Fig. 7. The contours of classical variables: (a) gas pressure; (b) gas temperature; (c) Mach number; and (d) liquid film temperature.

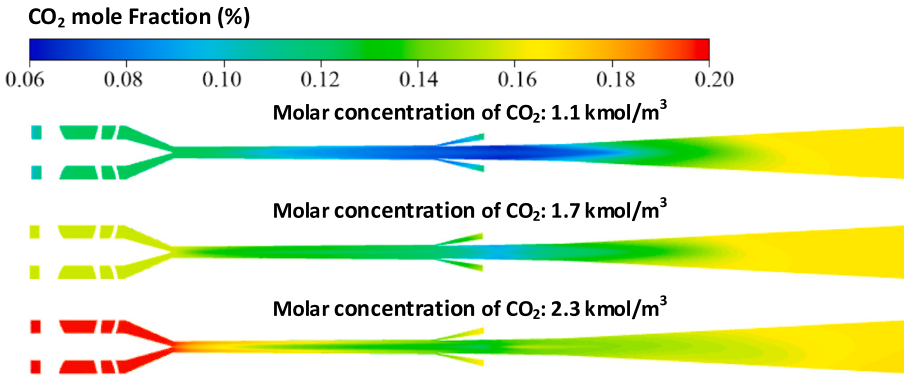

(a) Contour distribution of CO_2 mole fraction under different inlet CO_2 concentrations

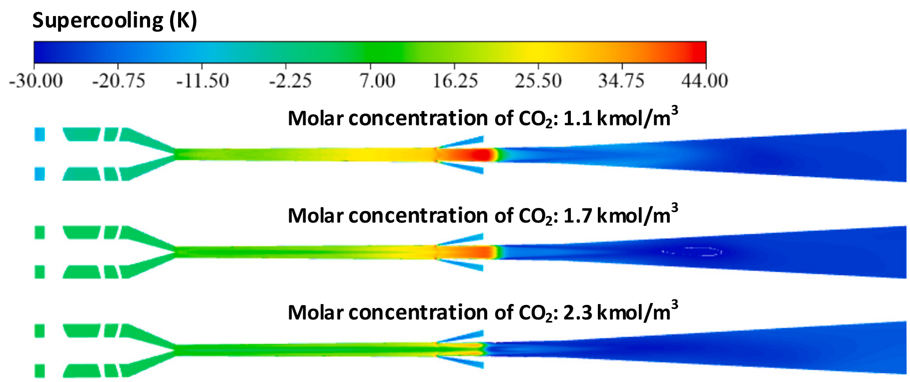

(b) Contour distribution of supercooling under different inlet CO_2 concentrations

Fig. 8. The contours of classical variables under different inlet CO_2 concentrations.

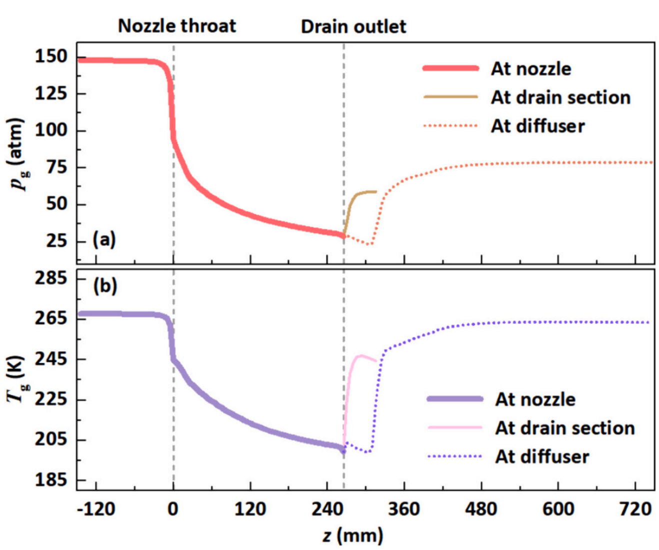

Fig. 9. The distribution of classical variables along the separator: (a) gas pressure; (b) gas temperature.

solution, supersonic separators should be designed to precipitate liquid CO_2 at appropriate temperatures [55]. Fig. 7(b) and Fig. 9(b) displays the temperature distribution within the y = 0 cross section of the supersonic separator. The variation in temperature indicates a small region near the drain outlet where the temperature falls below 217 K. Theoretically, this region exhibits properties of the solid-phase region of CO_2, resulting in the conversion of CO_2 droplets into dry ice. However, the wall temperature, the gas temperature in the boundary layer and the liquid film temperature, as shown in Fig. 7(d), are all higher than 217 K. The wall temperature is queried to be about 258 K, which is higher than the gas temperature, and there is heat exchange between the liquid film and the wall. That is to say, even a small quantity of dry ice generated in this area will promptly return to its liquid phase in proximity to the wall. Therefore, in the numerical model developed in this paper, the freeze-

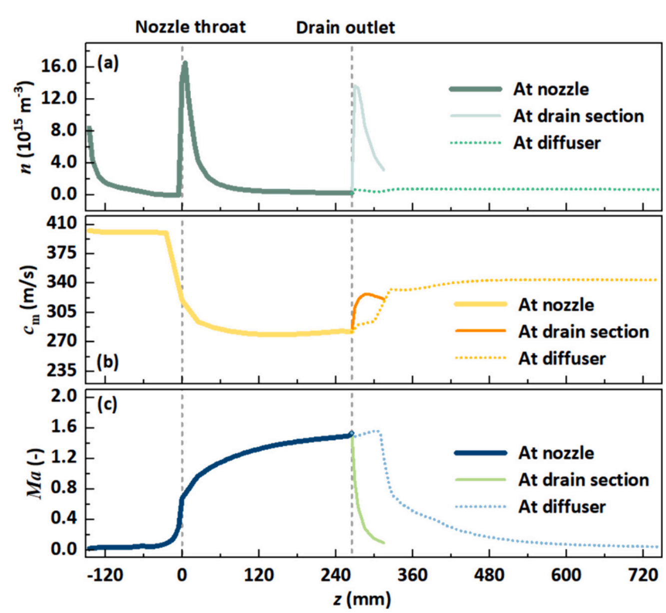

Fig. 10. The distribution of classical variables along the separator: (a) droplet number concentration; (b) sound speed; and (c) Mach number.

out of CO_2 is sensibly neglected.

Fig. 10(a) displays the droplet number concentration (homogeneous + heterogeneous). Only the heterogeneous droplets are present before the nozzle throat, due to the swirling motion, the heterogeneous droplets cling to the wall and their number per volume decreases progressively. Downstream from the throat, many homogeneous nuclei are produced by condensation, which grow and deposit rapidly. At the drain outlet, the shock wave caused the liquid film to strip and separate droplets, which increased in number before being quickly separated out. These changes above lead to changes in the liquid phase concentration, which affects the liquid phase sound speed and ultimately changes the mixture sound speed. Also, it is a well-established fact that the sound speed and Mach number have an inverse relationship, as illustrated in Fig. 10(b-c). On the basis of the above, overall, the gas pressure in the convergent section of the supersonic nozzle continues to expand, accompanied by a decrease in the static temperature and an increase in the Mach number. Once the gas reaches the throat of the supersonic nozzle, the Mach number hits 1.0, leading to a temperature decrease of about 30 K. The gas expands further through the convergent section of the supersonic nozzle and the diffuser with a progressively increasing Mach number. Once the Mach number reaches its peak of 1.6, the temperature decreases to a minimum value of 199.0 K. In the diffuser, the gas pressure and gas temperature undergo partial recovery, resulting in a corresponding decrease in the Mach number. Upon reaching the dry gas outlet, the gas pressure registers at 79.0 atm, while the temperature is 263.5 K, and the Mach number is reduced to 0.04. Therefore, from the qualitative aspect, the developed numerical model is accurate.

4. Mass, energy and economic analysis

The supersonic separator's ability to reduce carbon emissions was tested using the developed model that focused on two aspects: capturing the most CO_2 mass and minimizing energy waste. This assessment not only measured the separator's effectiveness at capturing CO_2, but also emphasized the importance of conserving energy during the separation process.

4.1. Utilization of mass transfer

First, the study focused on investigating the impact of foreign droplets on mass transfer. Fig. 11(a) shows the variation of CO_2 mole fraction in the flow field when only homogeneous condensation occurs, and it can be seen that the CO_2 mole fraction at the gas outlet is about 19.3%, which is not much different from the inlet. In contrast, Fig. 11(b) shows the combined effect of homogeneous/heterogeneous condensation on the flow field, where the outlet CO_2 mole fraction drops to about 16.7%, implying better carbon mass separation.

Further, Fig. 12 displays the CO_2 vapor mole fraction profile along the axial direction for varying heterogeneous droplet concentrations. For the case with only homogeneous droplets, the mole fraction of CO_2 vapor at the dry gas outlet of the supersonic separator is almost equal to that at the inlet. Nevertheless, the existence of heterogeneous droplets leads to the condensation of part of the carbon vapor on the heterogeneous nuclei. Heterogeneous nuclei typically have a larger diameter

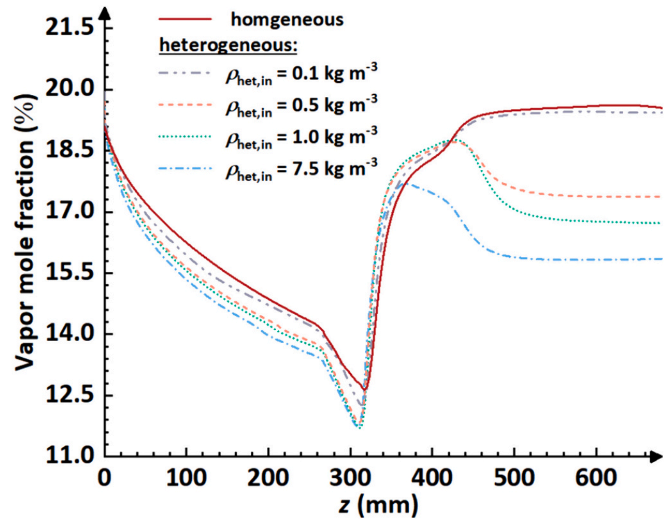

Fig. 12. Vapor mole fraction distribution under different $\rho_{het,in}$.

than homogeneous nuclei, resulting in a greater mass and higher probability of centrifugal separation. Correspondingly, heterogeneous droplets are more likely to contact the wall, deposit and separate, fulfilling the purpose of carrying vapors away from the supersonic separator in the form of droplets. Thus, in the presence of heterogeneous droplets, the CO_2 vapor mole fraction at the dry gas outlet is generally lower than in the case of homogeneous condensation alone. Furthermore, the molar fraction of carbon vapor at the outlet tends to reduce as the inlet heterogenous droplet concentration increases, indicating a greater separation of carbon dioxide.

A visual representation of the liquid film thickness evolution across varying heterogeneous droplet concentrations is presented in Fig. 13. When the gas containing swirling droplets flows into the nozzle

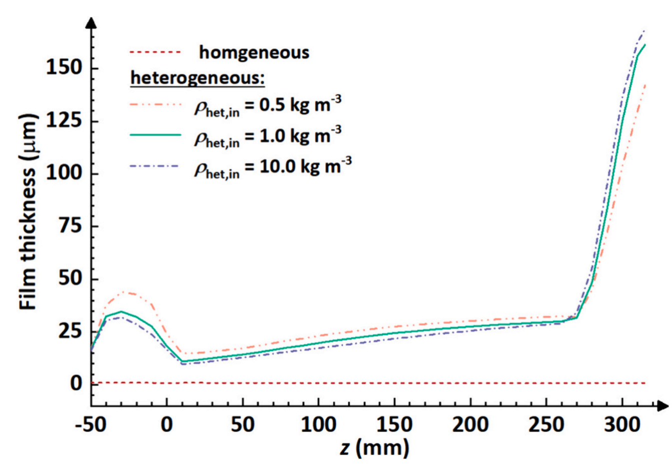

Fig. 13. Film thickness distribution under different $\rho_{het,in}$

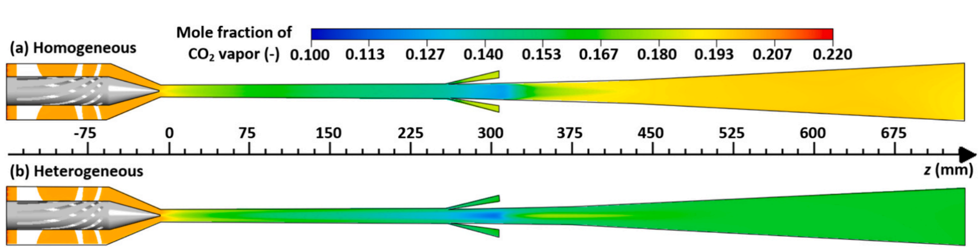

Fig. 11. Effect of the presence of foreign droplets on the mass transfer.

convergent section, due to centrifugal force, the swirling droplets move towards the wall, thus the liquid film begins to take shape. In the convergent section, the rapid increase in gas velocity leads to an increase in droplet and liquid film velocity. However, as the gas velocity increases to supersonic level, the liquid film velocity at the nozzle throat accelerates by <1 m s^{-1}. The high shear force results in the stripping of the liquid film. In the divergent section of the nozzle, droplets are continuously deposited and part of the water vapor condenses to form liquid film, so the thickness of the liquid film slowly increases. After the film enters the drain outlet, the effect of gas on the liquid film decreases. The film thickness will increase dramatically, although the evaporation behavior of the liquid film exists in this stage. Apparently, in a situation of homogeneous flow, the liquid film thickness approaches zero, indicating minimal droplet deposition on the wall surface and subsequent separation. As the concentration of heterogeneous droplets continues to increase, the thickness of the liquid film gradually increases. This trend is especially evident at the liquid outlet position, situated around 270 mm into the system. The liquid film thickness eventually achieves a substantial magnitude, reaching up to 168 μm in the case of $\rho_{het,in} = 10$ kg/m^3. This result implies an increased potential for large-scale utilization, as the increased liquid film thickness improves the likelihood of successful separation.

4.2. Utilization of energy transfer

The entropy generation of the supersonic separator are explored in this section. For the case of $\rho_{het,in} = 7.5$ kg/m^3, the entropy generation data of different cross sections on the divergent section of the supersonic nozzle were analyzed and compiled into Fig. 14. It can be seen from the data that with the increase of axial position, the values of total entropy production and four kinds of entropy production all increase, among which viscous entropy generation $s_{gen,D}$, phase change entropy generation $s_{gen,L}$ and aerodynamic entropy generation $s_{gen,A}$ occupy the main components. The entropy generation data four types regarding the $z =$ 260 mm cross-section were selected for further illustration. The total entropy generation of this cross-section is 0.529 kJ/(kg k), of which $s_{gen,A}$ accounts for 33.28%, $s_{gen,D}$ accounts for 48.60%, $s_{gen,L}$ accounts for 18.07%, and $s_{gen,C}$ is only 0.05%. That is to say, fluid viscosity, phase change and aerodynamic loss are the main factors leading to entropy generation in the nozzle expansion section of supersonic separator, which will cause irreversible energy loss.

The entropy generation due to phase change is mainly caused by homogeneous condensation and heterogeneous condensation, the values of entropy generation along the supersonic nozzle due to homogeneous and heterogeneous phase change are shown in Fig. 15. From the graph, it can be analyzed that both $s_{gen,hom}$ and $s_{gen,het}$ are showing a growing trend. But $s_{gen,hom}$ fluctuates between 0.001 kJ/(kg•K) and 0.002 kJ/(kg•K), while $s_{gen,het}$ grows from zero all the way up to 0.095 kJ/(kg•K). Numerically speaking, $s_{gen,het}$ is two orders of magnitude larger than $s_{gen,hom}$. Therefore, it can be concluded that the role played by heterogeneous condensation in the entropy production due to phase change accounts for a large part of it, while the role of homogeneous condensation is almost negligible.

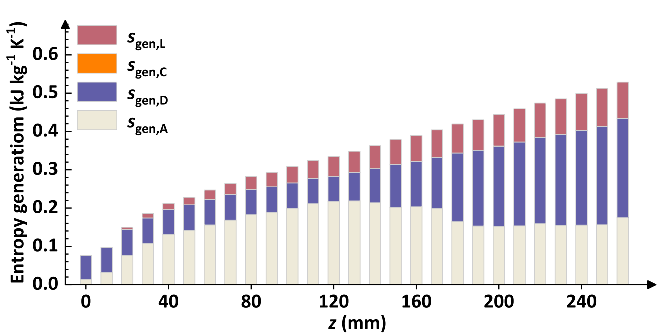

Fig. 14. Four types of entropy generation along the nozzle

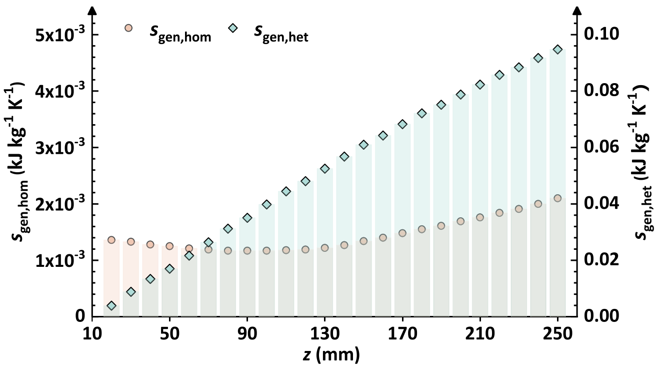

Fig. 15. Entropy generation due to homogeneous and heterogeneous phase change along the nozzle

When considering the influence of viscosity on entropy generation, a significant factor is the mean value of viscous dissipation, represented as $Y_{gen,\overline{D}}$. This value plays a crucial role in driving the overall increase in entropy. Fig. 16 provides a visual representation of how this energy dissipation is distributed across the flow field. From the diagram, it is apparent that there are four significant regions where the mean value of viscous dissipation $Y_{gen,\overline{D}}$ is prominently pronounced. These regions include the sharp corner of the cone, the near-wall region, the drain outlet region, and the diffuser section. This distribution pattern reveals potential inefficiencies in the present design of the supersonic separator. It suggests that there exists an opportunity for enhancement, particularly by optimizing the design of components like the drain outlet and cone. Refining these particular regions has the potential to enhance the separator configuration.

4.3. Mass and energy assessment

The effect of different $\rho_{het,in}$ on mass utilization was counted. The CO_2 vapor removal rate and the mass of separated CO_2 per second are two important indexes chosen in this study. Fig. 17 clearly showed the changing trend of the two indicators. As the $\rho_{het,in}$ increases from 0.1 kg/m^3 to 10 kg/m^3, both indicators show a trend of increasing and then decreasing, which can reach a maximum of 24.25% and 0.28 kg/s. With such a variation pattern, a $\rho_{het,in}$ of 5 kg/m^3 is expected to achieve the best quality utilization efficiency, but its energy consumption remains to be explored. Among them, the calculation method of CO_2 mass separated per second M_{CO2} is as follows:

$$M_{CO2} = q_{out}\left(\dot{Y}_{CO2,out} - \dot{Y}_{CO2,in}\right) \tag{33}$$

where q_{out}, $\dot{Y}_{CO2,in}$ and $\dot{Y}_{CO2,out}$ represent the outlet mass flow rate (kg/s) and mass fraction of the inlet and dry gas outlet inside the supersonic separator, respectively.

Additionally, two measures were selected to assess energy efficiency, which are the exergy destruction and the total entropy generation at the outlet. In Fig. 18(a), the impact of increasing $\rho_{het,in}$ ranging from 0.1 kg/m^3 to 10 kg/m^3 becomes evident. There is a clear tendency for both indicators to increase and then decrease, with peaks reaching 179.58 kJ/kg and 0.66 kJ/(kg•K) respectively when $\rho_{het,in}$ was 5 kg/m^3. This indicates that the more available energy is lost inside the supersonic separator due to irreversible processes, an indication of reduced energy efficiency. Here in Fig. 18(b) has the same trend. After calculation, the maximum values of 477.29 kW and 451.75 kW can be reached at a $\rho_{het,in}$ of 5 kg/m^3 and 7.5 kg/m^3 respectively, which also proves that the energy loss is the largest under these two concentrations. As shown in

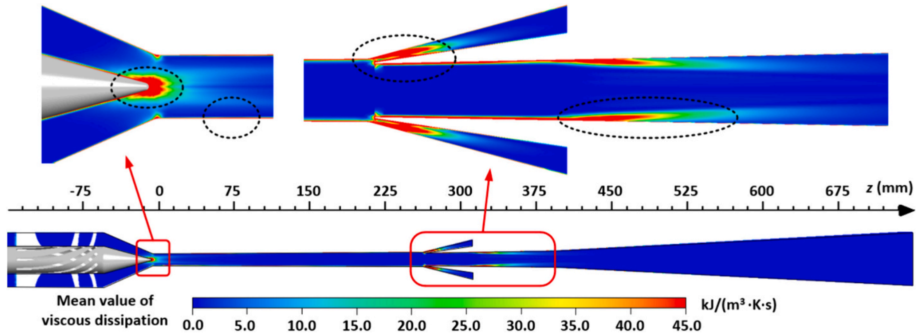

Fig. 16. Distribution of the mean value of viscous dissipation

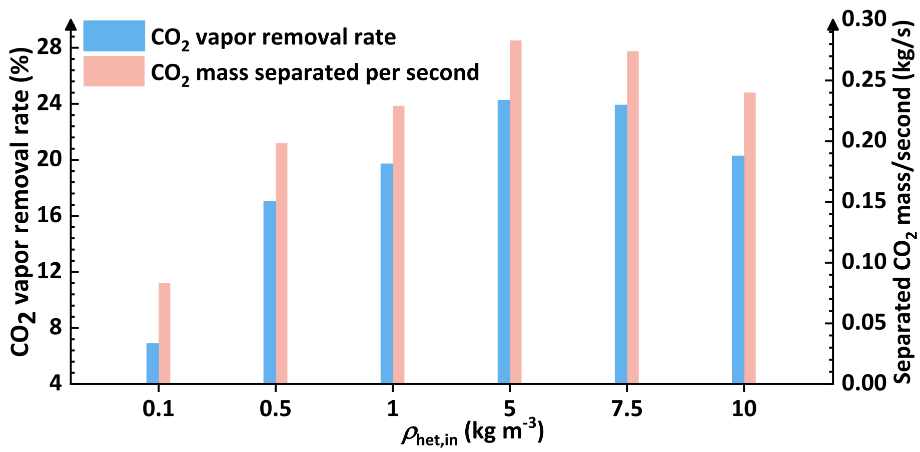

Fig. 17. Mass utilization under different $\rho_{het,in}$

Fig. 17, it is considered that the $\rho_{het,in}$ of 5 kg/m^3 has a better CO_2 mass separation performance. It can be seen that the mass separation performance and energy utilization performance are two contradictory evaluation parameters. Specifically, improving mass separation performance typically involves using more energy, while pursuing lower energy utilization may sacrifice mass separation performance. A combination of these two factors is critical in the design and optimization of supersonic separators. By continuing to calculate the energy consumption required for CO_2 separation per unit mass and time (Fig. 18 (b)), it can be found that the energy consumption per unit mass and time is lower at 7.5 kg/m^3. Therefore, it is expected to achieve a balance between mass and energy utilization between 5 kg/m^3 and 7.5 kg/m^3, which needs more calculation and validation.

The analysis of this study shows that there is still a lot of room for research on supersonic separators. First, the structure used in this study is not the best separation structure, and there must be better ways to make the viscous dissipation [56] relatively small. Second, it is currently difficult to obtain experimental data on supersonic separators, better intelligent detection methods need to be developed, as well as more field tests are needed for industrialization. Third, it is still worth exploring exactly what operating conditions provide the relatively best dual utilization of mass and energy for CO_2 capture, which requires a large amount of simulation and experimental data for a multi-target analysis. Finally, this technology has been applied on a certain scale by some international companies, mostly focusing on offshore natural gas extraction. Whether supersonic CO_2 capture technology alone or in combination with other CCUS technologies can have greater breadth and depth of application requires subsequent research and advancement by multiple parties [57].

4.4. Economic analysis

For cost analysis, this study summarizes the CO_2 purity and recovery by CO_2 capture and separation technology commonly used at present [58,59].

Supersonic low-temperature phase change separation technology in our study has no chemical reagents and does not involve additional pollution in the capture system. It has become a new green capture technology with great potential and application value. Cascade mode can effectively improve CO_2 recovery rate. According to the utilization of mass and energy by current supersonic separation technology, the removal rate of CO_2 can reach about 25% with the addition of single-stage separator, but the outlet pressure is still high enough for multi-stage separators. With the addition of multi-stage cascade, increasing pressure loss will bring greater CO_2 recovery. Table 6 below summarizes the economic parameters under different CO_2 separation technologies.

5. Conclusions

The main objective of this study was to investigate the feasibility of supersonic CO_2 capture technology, a novel CCUS method, for decarbonization. CO_2 capture in the natural gas extraction process was chosen as an entry point to study the condensation and separation of supercritical CO_2 in a CH_4-CO_2 binary system in a supersonic separator. The utilization of mass and energy by the CO_2 capture process in the supersonic separator was analyzed using a combination of the entropy transport equation and the Euler-Euler-Euler real gas model. The findings led to the following discoveries:

(1) For mass utilization, the presence of heterogeneous droplets allows more CO_2 vapor to condense into droplets and be thrown

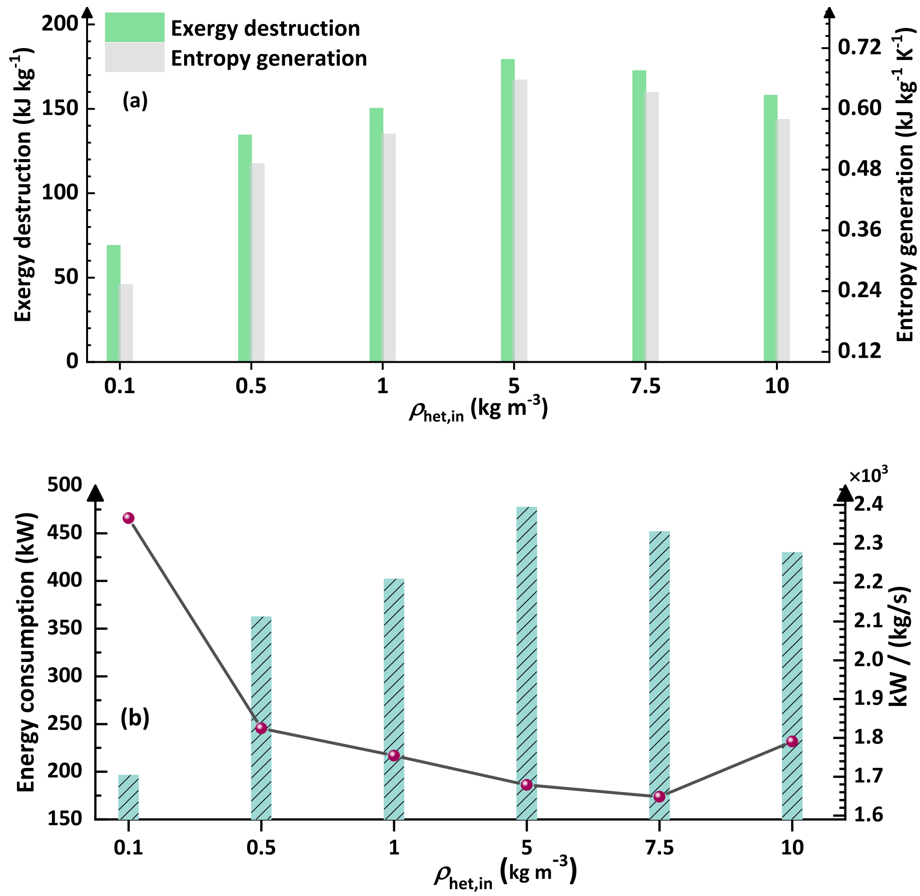

Fig. 18. (a) Energy utilization under different $\rho_{het,in}$; (b) Energy consumption under different $\rho_{het,in}$

Table 6
The key technical and economic parameters

CO_2 Separation Technology	CO_2 recovery (% vol.)	CO_2 purity (%)	Energy consumption (GJ/t CO_2)	Capture cost ($/t CO_2)
◆ Chemical absorption [60,61]	85–90	>95%	1.83–4.0	62.80
◆ Physical absorption [62,63]	88–95	>99%	2.4–9.0	89.66
◆ Membranes [64,65]	70–90	>95%	1.1–1.9	80.46
◆ Biological [66]	10–40	>99%	–	793
◆ Cryogenic [67,68]	90–99	>99%	0.85–3	52
◆ **Supersonic separator (SS)**	60–80	>99%	0.85–2	38
◆ **SS + absorption**	90–95	>99%	1.34–3	50.4

Notes: $ = USD
USD 1 = EUR 0.93

against the wall to form a liquid film, thus capturing a larger mass of CO_2.

(2) For energy utilization, viscosity, heterogeneous phase change, and aerodynamic loss are the three main factors leading to entropy generation, which account for 48.60%, 18.07% and 33.28% respectively, and the entropy generation due to heat conduction accounts for only 0.05%. And unreasonable structures such as sharp corner and drain outlet are the causes of large viscous dissipation.

(3) For the dual utilization of mass and energy, the results show that an inlet heterogeneous droplet concentration between 5 kg/m^3 and 7.5 kg/m^3 is expected to condense and separate the most CO_2 and require the least energy. The maximum recovery rate of CO_2 predicted by SS combined with absorption can reach 90%, while the minimum energy consumption is 1.34 GJ/t, and the cost can be lower than that of single adsorption method, which can be as low as 50.4 $/t.

The analysis of this study shows that there is still a lot of room for research on supersonic separators. This study also investigates and calculates the economic indicators of different CO_2 separation technologies. Whether supersonic CO_2 capture technology alone or in combination with other CCUS technologies can have greater breadth and depth of application requires subsequent research and advancement by multiple parties.

CRediT authorship contribution statement

Hongbing Ding: Writing – review & editing, Writing – original draft, Supervision, Methodology, Investigation, Funding acquisition, Conceptualization. **Yuanyuan Dong:** Writing – review & editing, Methodology. **Yu Zhang:** Writing – review & editing, Writing – original draft, Investigation, Formal analysis. **Chuang Wen:** Writing – review & editing, Supervision, Methodology, Investigation, Funding acquisition, Formal analysis. **Yan Yang:** Writing – review & editing, Supervision, Methodology, Investigation, Formal analysis.

Declaration of competing interest

The authors declared that there is no conflict of interest.

The authors declare that they have no known competing financial interests or personal relationships that could have appeared to influence the work reported in this paper.

Data availability

The research data supporting this publication are provided within this paper.

Acknowledgment

This work is supported by National Natural Science Foundation of China under Grant 52276159, 51876143 and 62073135, National Key Research and Development Program of China under Grant 2023YFB3209304, and the Engineering and Physical Sciences Research Council [grant number EP/X027147/1]. For the purpose of open access, the author has applied a 'Creative Commons Attribution (CC BY) licence to any Author Accepted Manuscript version arising'.

References

[1] Lakzian E, Yazdani S, Salmani F, Mahian O, Kim HD, Ghalambaz M, et al. Supersonic separation towards sustainable gas removal and carbon capture. Prog Energy Combust Sci 2024;103:101158.
[2] Singer G, Köll R, Aichhorn L, Pertl P, Trattner A. Utilizing hydrogen pressure energy by expansion machines–PEM fuel cells in mobile and other potential applications. Appl Energy 2023;343:121056.
[3] Osman A, Chen L, Yang M, Msigwa G, Farghali M, Fawzy S, et al. Cost, environmental impact, and resilience of renewable energy under a changing climate : a review. Environ Chem Lett 2022;21:741–64.
[4] Chen WH, Lu X, Lei YL, Chen JF. A comparison of incentive policies for the optimal layout of CCUS clusters in China ' s coal-fired power plants toward carbon neutrality. Engineering 2021;7:1692–5.
[5] Han JP, Li JC, Tang X, Wang LC, Yang XL, Ge ZQ, et al. Coal-fired power plant CCUS project comprehensive benefit evaluation and forecasting model study. J Clean Prod 2023;385:135657.
[6] Lin QY, Zhang X, Wang T, Zheng CH, Gao X. Technical Perspective of Carbon Capture, Utilization, and Storage. Engineering 2022;14:27–32.
[7] Zhang ZE, Wang T, Blunt MJ, Anthony EJ, Park AA, Hughes RW, et al. Advances in carbon capture, utilization and storage. Appl Energy 2020;278:115627.
[8] Nocito F, Dibenedetto A. Atmospheric CO2 mitigation technologies: carbon capture utilization and storage. Curr Opin Green Sustain Chem 2020;21:34–43.
[9] Yan JY, Zhang ZE. Carbon capture, utilization and storage (CCUS). Appl Energy 2019;235:1289–99.
[10] Chu FM, Yang LJ, Du XZ, Yang YP. Mass transfer and energy consumption for CO2 absorption by ammonia solution in bubble column. Appl Energy 2017;190:1068–80.
[11] Zhang Z, Cai JC, Chen F, Li H, Zhang WX, Qi WJ. Progress in enhancement of CO2 absorption by nanofluids: a mini review of mechanisms and current status. Renew Energy 2018;118:527–35.
[12] Zhao RK, Zhao L, Deng S, Song CF, He JN, Shao YW, et al. A comparative study on CO2 capture performance of vacuum-pressure swing adsorption and pressure-temperature swing adsorption based on carbon pump cycle. Energy (Oxf) 2017;137:495–509.
[13] Petrovic B, Gorbounov M, Masoudi Soltani S. Impact of surface functional groups and their introduction methods on the mechanisms of CO2 adsorption on porous carbonaceous adsorbents. Carbon Capture Sci & Technol 2022;3:100045.
[14] Castro-Muñoz R, Zamidi Ahmad M, Malankowska M, Coronas J. A new relevant membrane application: CO2 direct air capture (DAC). Chem Eng J 2022;446:137047.
[15] Brunetti A, Scura F, Barbieri G, Drioli E. Membrane technologies for CO2 separation. J Membr Sci 2010;359:115–25.
[16] Yamasaki H, Wakimoto H, Kamimura T, Hattori K, Neksa P, Yamaguchi H. Visualization and measurement of swirling flow of dry ice particles in cyclone separator-Sublimator. Energies (Basel) 2022;15:4128.
[17] Song C, Liu Q, Deng S, Li H, Kitamura Y. Cryogenic-based CO2 capture technologies: state-of-the-art developments and current challenges. Renew Sust Energ Rev 2019;101:265–78.
[18] Wen C, Cao XW, Yang Y, Zhang J. Effects of swirls on natural gas flow in supersonic separators. The twenty-first international offshore and polar. Engineering Conference 2011:11–592.
[19] Shoghl SN, Naderifar A, Farhadi F, Pazuki G. A novel strategy for comprehensive optimization of structural and operational parameters in a supersonic separator using computational fluid dynamics modeling. Sci Rep 2021;11:21850.
[20] Interlenghi SF, de Medeiros JL, Araújo ODQF. On small-scale liquefaction of natural gas with supersonic separator: energy and second law analyses. Energy Convers Manag 2020;221:113117.
[21] Schinkelshoek P. Epsom H. Supersonic gas conditioning-low pressure drop twister for NGL recovery 2006;17884.
[22] Feygin V, Imayev S, Alfyorov V, Bagirov L, Dmitriev L, Lacey J. Supersonic gas technologies. Calgary, Canada: Translang Technologies Ltd; 2006. p. 166221459.
[23] Karimi A. Abdi MA. Selective removal of water from supercritical natural gas 2006;100442.
[24] Wen C, Cao XW, Yang Y, Li WL. An unconventional supersonic liquefied technology for natural gas. Energy Education Science and Technology Part a: Energy Science and Research 2012;30:651–60.
[25] Wen C, Ding HB, Yang Y. Optimisation study of a supersonic separator considering nonequilibrium condensation behaviour. Energy Convers Manag 2020;222:113210.
[26] Liu HW, Liu Z, Feng YX, Gu KY, Yan TM. Characteristics of a supersonic swirling dehydration system of natural gas. Chin J Chem Eng 2005;13:9–12.
[27] Haghighi M, Hawboldt KA, Abedinzadegan Abdi M. Supersonic gas separators: review of latest developments. J Nat Gas Sci Eng 2015;27:109–21.
[28] Wen C, Cao X, Yang Y, Zhang Y, Zhang J, Wang G. A dehydration experiment on a new-style supersonic swirling separator. Acta Pet Sin 2012;33:310–4.
[29] Ding HB, Sun CQ, Wen C, Liang ZX. The droplets and film behaviors in supersonic separator by using three-field two-fluid model with heterogenous condensation. Int J Heat Mass Transf 2022;184:122315.
[30] Liu Y, Cao XW, Yang J, Li YX, Bian J. Energy separation and condensation effects in pressure energy recovery process of natural gas supersonic dehydration. Energy Convers Manag 2021;245:114557.
[31] Shooshtari SHR, Shahsavand A. Optimal operation of refrigeration oriented supersonic separators for natural gas dehydration via heterogeneous condensation. Appl Therm Eng 2018;139:76–86.
[32] Bai BF, Li X, Li SQ. Computation of supersonic branching flow with Aerosol particle separation. AIAA J 2016;54:2069–76.
[33] Wang YG, Yu Y, Hu DP, Xu DX, Yi LY, Zhang Y, et al. Improvement of drainage structure and numerical investigation of droplets trajectories and separation efficiency for supersonic separators. Chem Eng Process Process Intensif 2020;151:107844.
[34] Han JQ, Feng JM, Hou TF, Chen W, Peng XY. Numerical and experimental study on gas-water separators for a PEMFC system. Int J Green Energy 2021;18:490–502.
[35] Chen WZ, Chen Y, Zhang WM, He SW, Li B, Jiang JZ. Paint thickness simulation for robotic painting of curved surfaces based on Euler–Euler approach. J Braz Soc Mech Sci Eng 2019;41:199.
[36] Yue T, Chen JY, Song JF, Chen XH, Wang YA, Jia ZH, et al. Experimental and numerical study of upper swirling liquid film (USLF) among gas-liquid cylindrical cyclones (GLCC). Chem Eng J 2019;358:806–20.
[37] Deng YJ, Zhang L, Hou H, Yu B, Sun DL. Modeling and simulation of the gas-liquid separation process in an axial flow cyclone based on the Eulerian-Lagrangian approach and surface film model. Powder Technol 2019;353:473–88.
[38] Ding HB, Zhang Y, Yang Y, Wen C. A modified Euler-Lagrange-Euler approach for modelling homogeneous and heterogeneous condensing droplets and films in supersonic flows. Int J Heat Mass Transf 2023;200:123537.
[39] Ding HB, Zhang Y, Dong YY, Wen C, Yang Y. High-pressure supersonic carbon dioxide (CO2) separation benefiting carbon capture, utilisation and storage (CCUS) technology. Appl Energy 2023;339:120975.
[40] Zhou L, Hang J, Bai L, Krzemianowski Z, El-Emam MA, Yasser E, et al. Application of entropy production theory for energy losses and other investigation in pumps and turbines: a review. Appl Energy 2022;318:119211.
[41] Arinelli LD, de Medeiros JL, de Melo DC, Teixeira AM, Brigagao GV, Passarelli FM, et al. Carbon capture and high-capacity supercritical fluid processing with supersonic separator: natural gas with ultra-high CO_2 content. J Nat Gas Sci Eng 2019;66:265–83.
[42] Arinelli LD, Teixeira AM, de Medeiros JL, Araújo O. Supersonic separator for cleaner offshore processing of natural gas with high carbon dioxide content: environmental and economic assessments. J Clean Prod 2019;233:510–21.
[43] Dutta T, Sinhamahapatra KP, Bandyopadhyay SS. Numerical investigation of gas species and energy separation in the Ranque–Hilsch vortex tube using real gas model. Int J Refrig 2011;34:2118–28.
[44] Matheis J, Müller H, Lenz C, Pfitzner M, Hickel S. Volume translation methods for real-gas computational fluid dynamics simulations. J Supercrit Fluids 2016;107:422–32.
[45] Zhao MR, Zhao YY, Pei JZ, Yang QC, Liu GB, Li LS. Research on non-equilibrium condensation of supercritical carbon dioxide in sCO2 power systems. Appl Therm Eng 2023;233:121215.
[46] Yuan SX, Fan YG, Chen B, Li JM, Gao L, Zhang S. Forming and stripping of the wall film and the influence on gas-liquid separation. Asia Pac J Chem Eng 2020;15(3):e2447.
[47] Wang XM, Chang HJ, Corradini M, Cong TL, Wang J. Prediction of falling film evaporation on the AP1000 paSsive containment cooling system using ANSYS FLUENT code. Ann Nucl Energy 2016;95:168–75.
[48] Kantrowitz A. Nucleation in very rapid vapor expansions. J Chem Phys 1951;19:1097–100.
[49] Moore MJ. Two-phase steam flow in turbines and separators: theory, instrumentation, engineering. Hemisphere Publishing Co.; 1976.
[50] Ding HB, Li Y, Lakzian E, Wen C, Wang C. Entropy generation and exergy destruction in condensing steam flow through turbine blade with surface roughness. Energy Convers Manag 2019;196:1089–104.
[51] Lettieri C, Paxson D, Cross PB, Spakovszky Z. Characterization of nonequilibrium condensation of supercritical carbon dioxide in a de Laval nozzle. J Eng Gas Turbines Power 2017;140:41701.
[52] Arinelli LD, Brigagao GV, Wiesberg IL, Teixeira AM, de Medeiros JL, Araújo O. Carbon-dioxide-to-methanol intensification with supersonic separators: extra-

carbonated natural gas purification via carbon capture and utilization. Renew Sust Energ Rev 2022;161:112424.

[53] Li HY, Vasquez SA, ASME. Numerical simulation of steady and unsteady compressible multiphase flows. Proceedings of the Asme International Mechanical Engineering Congress and Exposition-2012, Vol 7, Pts a-D. 2013. 2239–2251.

[54] Teixeira AM, Arinelli LD, de Medeiros JL, Araújo O. Sustainable offshore natural gas processing with thermodynamic gas-hydrate inhibitor reclamation: supersonic separation affords carbon capture. Chem Eng Res Des 2022;181:55–73.

[55] Arinelli LD, Trotta T, Teixeira AM, de Medeiros JL, Araújo O. Offshore processing of CO_2 rich natural gas with supersonic separator versus conventional routes. J Nat Gas Sci Eng 2017;46:199–221.

[56] Ding H, Dong Y, Zhang Y, Wen C, Yang Y. Exergy performance analysis of hydrogen recirculation ejectors exhibiting phase change behaviour in PEMFC applications. Energy (Oxford) 2024;300:131563.

[57] Lakzian E, Yazdani S, Salmani F, Mahian O, Kim HD, Ghalambaz M, et al. Supersonic separation towards sustainable gas removal and carbon capture. PROG ENERG COMBUST 2024;103:101158.

[58] Hong WY. A techno-economic review on carbon capture, utilisation and storage systems for achieving a net-zero CO2 emissions future. Carbon Capture Sci & Technol 2022;3:100044.

[59] Dziejarski B, Krzyżyńska R, Andersson K. Current status of carbon capture, utilization, and storage technologies in the global economy: a survey of technical assessment. Fuel (Guildford) 2023;342:127776.

[60] Guo H, Li C, Shi X, Li H, Shen S. Nonaqueous amine-based absorbents for energy efficient CO2 capture. APPL ENERG 2019;239:725–34.

[61] Shen Y, Jiang C, Zhang S, Chen J, Wang L, Chen J. Biphasic solvent for CO2 capture: amine property-performance and heat duty relationship. APPL ENERG 2018;230:726–33.

[62] Shi Z, Tao Y, Wu J, Zhang C, He H, Long L, et al. Robust Metal–Triazolate Frameworks for CO2 Capture from Flue Gas. J Am Chem Soc 2020;142:2750–4.

[63] Pardakhti M, Jafari T, Tobin Z, Dutta B, Moharreri E, Shemshaki NS, et al. Trends in solid adsorbent materials development for CO2 capture. ACS APPL MATER INTER 2019;11:34533–59.

[64] Yuan M, Narakornpijit K, Haghpanah R, Wilcox J. Consideration of a nitrogen-selective membrane for postcombustion carbon capture through process modeling and optimization. J MEMBRANE SCI 2014;465:177–84.

[65] Song C, Liu Q, Ji N, Deng S, Zhao J, Li Y, et al. Reducing the energy consumption of membrane-cryogenic hybrid CO2 capture by process optimization. Energy (Oxford) 2017;124:29–39.

[66] Shen M, Tong L, Yin S, Liu C, Wang L, Feng W, et al. Cryogenic technology progress for CO2 capture under carbon neutrality goals: a review. Sep Purif Technol 2022;299:121734.

[67] Mehrpooya M, Esfilar R, Moosavian SMA. Introducing a novel air separation process based on cold energy recovery of LNG integrated with coal gasification, transcritical carbon dioxide power cycle and cryogenic CO2 capture. J Clean Prod 2017;142:1749–64.

[68] Liu B, Yang X, Chiang P, Wang T. Energy consumption analysis of cryogenic-membrane hybrid process for CO2 capture from CO2-EOR extraction gas. Aerosol Air Qual Res 2020;20:820–32.